Materials Advances

ROYAL SOCIETY OF CHEMISTRY

PAPER

Published on 28 July 2026

Cite this: DOI: 10.1039/d6ma00781c

Impact of framework topologies on CO_2 adsorption and transport properties in Zr-fumarate metal–organic frameworks and their mixed-matrix membranes

Virginia Guiotto,†[a] Elisa Carignani,†[bc] Letizia Trovarelli,[d] Martina Vaccaro,[ef] Francesco Della Croce,[b] Siria Bertolozzi,[b] Mariolino Carta,[gh] C. Grazia Bezzu,[g] Alessio Fuoco,[e] Ferdinando Costantino,*[d] Lucia Calucci*[bc] and Valentina Crocellà*[a]

Herein, we present a comparative study aimed at disclosing the role of framework topologies and pore chemical environments in governing the CO_2 adsorption, dynamics and transport properties of the two most widely used fumarate-based Zr-MOFs, namely, MOF-801 and MIP-203. The two MOFs were synthesized under the conditions reported in the literature, and their CO_2 adsorption properties were determined *via* volumetric gas sorption. The CO_2-loaded samples were studied using *ex situ* powder X-ray diffraction (PXRD) and multinuclear solid-state NMR (SSNMR) spectroscopy, revealing different interactions and dynamics of the adsorbed molecules within the two distinct frameworks, with MIP-203 exhibiting stronger confinement effects and restricted CO_2 motion, in contrast to the isotropic dynamics observed in MOF-801. To bridge molecular-scale behaviour with macroscopic performance in CO_2 capture and separation, both MOFs were employed as fillers for the preparation of mixed-matrix membranes (MMMs) based on a polymer of intrinsic microporosity, PIM-1. The CO_2 transport properties of the two MMMs were evaluated by combining permeation/diffusivity measurements with the SSNMR analysis. The distinct CO_2 dynamics in the pristine MOFs were preserved within the MMMs. Notably, the incorporation of MIP-203 into PIM-1 led to enhanced permeability, primarily driven by an increase in the diffusion coefficient with respect to MOF-801. These findings highlight how different connectivities and pore environments in MOFs affect CO_2 behaviour, from its interaction with the framework to its transport in membranes.

Received 27th May 2026,
Accepted 28th July 2026

DOI: 10.1039/d6ma00781c

rsc.li/materials-advances

Introduction

The chemistry of metal–organic frameworks (MOFs) has undergone significant expansion in recent years, with increasing focus on its implementation in real-world applications, especially for carbon dioxide capture and separation.[1] However, several requirements for the practical industrial deployment of MOFs, such as improved scalability, low production costs and environmental impacts, high availability of raw materials, and long-term stability under operating conditions, still represent major bottlenecks for their widespread application.

Zr-based MOFs offer significant advantages in the realm of gas separation due to their high hydrothermal stability, environmentally friendly synthesis protocols and good CO_2 adsorption properties.[2] In particular, Zr-MOFs based on simple C_4 dicarboxylic ligands such as fumaric acid and its analogues (*e.g.* aspartic acid, succinic acid, malic acid, and mesaconic acid) have been largely developed in the past few years.[3,4] Among them, MOF-801, based on fumaric acid and isoreticular to UiO-66, is one

[a] *Department of Chemistry, NIS Reference Centre, INSTM Research Unit, University of Turin, Via G. Quarello 15/A and Via P. Giuria 7, 10125 Torino, Italy. E-mail: valentina.crocella@unito.it*
[b] *National Research Council of Italy – Institute of Chemistry of OrganoMetallic Compounds (CNR-ICCOM), Via G. Moruzzi 1, 56124 Pisa, Italy. E-mail: lucia.calucci@cnr.it, lucia.calucci@pi.iccom.cnr.it*
[c] *Center for Instrument Sharing University of Pisa (CISUP), Lungarno Pacinotti 43/44, 56126 Pisa, Italy*
[d] *Department of Chemistry, Biology e Biotechnologies (DCBB), INSTM research Unit, University of Perugia, 061233 Perugia, Italy. E-mail: ferdinando.costantino@unipg.it*
[e] *National Research Council of Italy – Institute on Membrane Technology "Enrico Drioli" (CNR-ITM), Via P. Bucci 17/C, 87036 Rende (CS), Italy*
[f] *Department of Chemical Sciences, University of Padua, Via Marzolo 1, 35131 Padua, Italy*
[g] *Department of Chemistry, Faculty of Science and Engineering, Swansea University, Singleton Park, Swansea SA28PP, UK*
[h] *Instituto de Síntesis Química y Catálisis Homogènea, Facultad de Ciencias, CSIC-Universidad de Zaragoza, C/Pedro Cerbuna 12, Zaragoza 50009, Spain*
† These authors contributed equally.

of the most extensively studied systems. It consists of 12-connected hexanuclear Zr_6 clusters, with the general formula of $Zr_6[\mu_3\text{-}O]_4[\mu_3\text{-}OH]_4[\text{fumarate}]_6$. Under certain synthesis conditions, however, structural defects can form, leading to a partial replacement of fumarate linkers with water, OH/Cl groups, acetate or formate.[5–7] Over the years, MOF-801 has been investigated for a wide range of applications, including water harvesting,[8] gas separation/capture,[9] pollutant removal,[10] catalysis,[11] and drug delivery.[12] In 2021, Butova *et al.* developed a fast (2 hour) and scalable synthesis of MOF-801, further enhancing its technological relevance.[13] Moreover, MOF-801 has been exploited as a promising filler for the design and fabrication of mixed-matrix membranes (MMMs),[14–16] demonstrating potential for CO_2 separation processes as well as in the fabrication of pure MOF membranes supported on $\alpha\text{-}Al_2O_3$ porous tubes.[17]

In parallel, Wang *et al.* reported the synthesis of a novel family of Zr-based MOFs with the general formula of $Zr_6[\mu_3\text{-}O]_4[\mu_3\text{-}OH]_4[L]_4[\text{formate}]_2[OH]_2[H_2O]_2$, where L represents C_4 dicarboxylate ligands such as fumarate, malate, or succinate, collectively referred to as MIP-203.[18] These new materials form 1D porous structures arising from the propagation of the secondary building units (SBUs), interconnected by formate anions, along the *c* direction. The C_4 linkers are linked to Zr atoms bridging the SBU in the *ab* planes. The hexanuclear clusters are 10-connected through eight independent fumarate linkers, two bridging formate anions, two μ_3-O groups, and an apical –OH group directed towards the channel. Owing to different connectivities, despite sharing the same precursors, MOF-801 and MIP-203 offer distinct structural and dynamic properties. All MIP-203 MOFs, including the fumarate-based analogue, display a degree of framework flexibility, namely, a slight expansion of the unit cell, when exposed to external *stimuli* such as adsorption of water and other solvents or CO_2 adsorption.[18]

Differences in the topology and framework flexibility between MOF-801 and MIP-203 may have an impact on their CO_2 adsorption and diffusion properties. Although some studies have already addressed their similarities and discrepancies,[18,19] a comprehensive correlation among the framework topology and CO_2 adsorption interaction is still missing.

The present work highlights the role of the SBU connectivity and the pore chemical environment in governing the CO_2 adsorption capability and mechanism of adsorption in MOF-801 and MIP-203. By combining *ex situ* powder X-ray diffraction (PXRD) and solid-state NMR (SSNMR) spectroscopy under a CO_2 atmosphere, new insights into the host–guest interactions and dynamics of CO_2 in the two MOFs are gained. These findings lay the foundation for the assessment of the performance of the two MOFs when they are used as fillers in MMMs based on a polymer of intrinsic microporosity, namely PIM-1, thus allowing molecular-scale properties to be correlated with macroscopic CO_2 separation and transport properties.

Experimental section

Materials

Zirconium chloride ($ZrCl_4$), formic acid, and fumaric acid were purchased from Sigma Aldrich and used as received without further purification. The gases used for permeation measurements (H_2, He, O_2, N_2, CH_4, and CO_2) were supplied by Sapio (Italy) at a minimum purity of $>99.9995\%$. Carbon-13-enriched CO_2 (99 atom%) for SSNMR experiments was purchased from Merck.

Syntheses of MOFs

MOF-801 was synthesised by adding formic acid (7.6 mL) into an aqueous solution (36.4 mL) of zirconium chloride ($ZrCl_4$) (2 mmol) and fumaric acid (6 mmol) in a Teflon-lined stainless-steel autoclave (inner Teflon beaker volume of *ca.* 50 mL). The mixture of reagents was first sonicated for 10 min in an ultrasonic bath, placed in an oven, maintained at 393 K for 24 h, and then cooled down to room temperature (RT). The obtained solid was washed with methanol (2×20 mL, 3 h). Finally, the solid was recovered by centrifugation and dried at 313 K overnight.

MIP-203 was prepared by adding zirconium chloride (2 mmol) to a solution of fumaric acid (1 mmol) and dissolving the mixture in 5 mL of formic acid. The resulting solution was sonicated for 10 min, transferred into a Teflon-lined stainless steel autoclave (inner Teflon beaker volume of *ca.* 25 mL) and then maintained at 393 K for 72 h. The solid was washed with ethanol and water (2×20 mL, 3 h), and finally, recovered by centrifugation and dried at 313 K overnight.

Synthesis of PIM-1

PIM-1 was synthesised according to the original low-temperature method.[20] A mixture of 5,5',6,6'-tetrahydroxy-3,3,3',3'-tetramethyl-1,1-spirobisindan (6.00 g; 17.63 mmol), 2,3,5,6-tetrafluoroterephthalonitrile (3.53 g; 17.63 mmol) and 19.5 g of anhydrous K_2CO_3 (141 mmol) was stirred in 115 mL of anhydrous dimethylformamide (DMF) for 96 h at 338 K. The reaction mixture was poured into water and a yellow precipitate was collected by filtration. The crude polymer was precipitated from a tetrahydrofuran (THF) solution into acetone first and then into methanol to give 6.60 g (yield 81%) of pure polymer. The product was analysed by ^1H NMR ($CDCl_3$), FT-IR (solid), TGA and N_2 adsorption at 77 K, and the data were perfectly in agreement with those reported in the literature.[20]

Preparation of MMMs

MMMs containing 10 wt% of the MOFs were prepared by casting the films from chloroform ($CHCl_3$), from a 3 wt/vol% polymer solution. PIM-1 and MOF-801 (or MIP-203) in powder form were first heated at 353 K in a vacuum oven overnight. PIM-1 (0.5 g) was solubilized in $CHCl_3$ (15 mL) and stirred overnight. Then 0.05 g of MOF was added, and the mixture was sonicated for 2 h using a QSONICA probe sonicator, which was set at amplitude 50, in pulse mode, 2 s on and 2 s off. The membranes were cast by slow evaporation from a Teflon Petri dish of 7.5 cm diameter.

Powder X-ray diffraction (PXRD)

The PXRD patterns in a controlled atmosphere were collected using a PANalytical X'Pert diffractometer with CuKα radiation

transmission geometry and equipped with an X′celerator strip detector. The sample was loaded in a borosilicate glass capillary tube (internal diameter = 0.5 mm). The diffractogram of the evacuated MIP-203 was recorded after degassing the capillary with a vacuum pump (residual pressure $<10^{-4}$ mbar) and heating it up to 373 K overnight. In a second capillary tube, 0.5 bar of CO_2 was dosed on the activated MIP-203 before collecting another PXRD pattern.

Field emission scanning electron microscopy (FE-SEM) and energy-dispersive X-ray spectroscopy (EDS)

Field emission SEM images of MOFs were acquired using a FE-LEO 1525 Gemini SEM (Zeiss/LEO) at an accelerating voltage of 5.00 kV (USA). The sample was sputter-coated under a vacuum with chromium. MMM images were acquired using a TESCAN S9000G FESEM 3010 microscope (30 kV), equipped with a Schottky-type FEG source. Prior to analysis, the samples were metalized with a chromium layer. Elemental mapping was performed on MMMs using an energy-dispersive X-ray spectroscopy detector (Oxford-Detector, equipped with the AZTEC software).

Gas sorption measurements

N_2 adsorption–desorption isotherms were collected at 77 K using a Micromeritics 3FLEX sorption analyser. Approximately 30 mg of powder was weighed and activated under dynamic vacuum at 373 K overnight (heating ramp of 3 K min^{-1}) prior to analysis. The Brunauer–Emmett–Teller specific surface area (SSA_{BET}) was evaluated in the 2×10^{-3}–2×10^{-2} p/p_0 range by following the Rouquerol consistency criteria.[21] The analysis of the pore size distribution (PSD) and cumulative pore volume (CPV) was performed by applying the non-local density functional theory (NL-DFT) method using the MicroActive Software provided by Micromeritics. For both MOFs, a slit pore geometry was assumed and the "HS-2D-NLDFT, Carbon, N_2, 77K" model was employed for the analysis. The microporous volume and microporous area were calculated by the *t*-plot method by applying the Harkins and Jura model. The isotherm was fitted in the thickness range between 3.5 and 5 Å.

The pore size distribution was also evaluated theoretically by using the ZEO++ software, which provides a geometry-based analysis of the void space from the crystallographic structures (.cif files) provided by the Cambridge Crystallographic Data Centre (CCDC). For both materials, the pore size distribution was calculated using 50 000 sampling points and a histogram comprising 1000 bins with a bin size of 0.1 Å. The optimal probe radius was set to 1.5 Å for MOF-801 and to 1.6 Å for MIP-203, and the calculations were performed using the high accuracy mode.

CO_2 adsorption–desorption isotherms at 273 K were acquired using the same instrument. Isothermal conditions were maintained using a chiller dewar from Micromeritics, in which a circulating coolant or heating fluid, regulated by a thermostatic bath (JULABO F25), ensured precise temperature control throughout the measurements.

Solid-state NMR spectroscopy (SSNMR)

SSNMR experiments were performed using a Bruker Avance NEO 500 spectrometer operating at Larmor frequencies of 500.13 MHz and 125.77 MHz for ^1H and ^{13}C, respectively. The spectrometer was equipped with a 4 mm double-channel (H/F-X) cross polarization/magic angle spinning (CP/MAS) probe. The 90° pulse length was 2.95 μs for ^1H and 4.10 μs for ^{13}C. ^1H direct excitation (DE) MAS spectra were acquired with 16 scans, with a recycle delay of 2–5 s, individually optimized for each experiment. ^1H–^{13}C CP MAS spectra with proton high-power decoupling were recorded for all samples with contact times ranging from 0.1 to 8 ms and accumulating 160–800 scans. The recycle delay, ranging from 1 to 3 s, was based on the optimized ^1H relaxation time. ^1H DE MAS and ^1H–^{13}C CP MAS measurements were carried out at 298 K using a spinning frequency of 15 kHz. ^{13}C DE spectra were recorded on the $^{13}CO_2$-loaded MOF samples under two sets of conditions: (i) at 298 K with a MAS frequency of 15 kHz and (ii) under static conditions at variable temperatures ranging from 268 to 338 K for MIP-203 and from 243 to 298 K for MOF-801. All spectra were acquired with a recycle delay of 5 s and 16–200 scans. For MMMs, ^{13}C DE static spectra were recorded at 298 K on $^{13}CO_2$-loaded samples with a recycle delay of 5 s and accumulating 6400 scans. ^1H–^{13}C HETCOR spectra with FSLG homonuclear decoupling and MAS frequency of 15 kHz were acquired on activated and $^{13}CO_2$-loaded MIP-203, using a recycle delay of 1 s and contact times of 0.2 and 2 ms. For each of the 128 increments in the indirect dimension, 200 scans were accumulated. Dry air was used as spinning and heating/cooling gas. Chemical shifts were referenced to the signal of adamantane at 37.77 ppm for ^{13}C and calculated for the other nuclei using the unified scale recommended by IUPAC.[22] The spectra were processed using the TopSpin Bruker software or MestreNova software.

Samples for SSNMR measurements were prepared by packing the MOF powders or the membranes cut in pieces into 4 mm outer diameter zirconia rotors. Activated samples were obtained by heating up at 373 K under dynamic vacuum (0.1 mbar) for 4–12 h. After activation, the rotors were capped under a N_2 atmosphere in a glove box. $^{13}CO_2$-loaded samples were prepared using a homemade cell equipped with a mechanical lever operated from outside that enables the capping of the rotor without disturbing the cell atmosphere. The activated samples were exposed to $^{13}CO_2$ (carbon-13 isotopically enriched CO_2; Merck, 99% ^{13}C atoms) at a pressure of 1 bar. Once the adsorption equilibrium was reached, the rotors were closed under the $^{13}CO_2$ atmosphere.

The NMR Weblab software[23] was used to simulate the line shape of ^{13}C static spectra of $^{13}CO_2$. The principal components of the chemical shift tensor used as input parameters in the software were $\delta_{11} = \delta_{22} = 232.7$ ppm and $\delta_{33} = -90.1$ ppm according to the measurements on solid CO_2.[24,25]

Measurement of gas transport properties

Prior to pure-gas permeation measurements, the residual solvent was removed and the casting history of the MMMs was erased by soaking the membranes in methanol for 24 h, followed by drying for additional 24 h, as commonly reported in the literature.[26] MMMs for aging studies were stored under ambient conditions, without controlling humidity or air

exposure and tested after approximately 30 and 90 days to assess the effect of physical aging on gas transport properties. Pure gas permeation tests on self-standing defect-free MMMs were carried out at 308 K and at a feed pressure of 1 bar using a fixed volume/pressure increase described elsewhere.[27] Before analysis, circular membrane samples were carefully evacuated for sufficient time (>1 h) with a turbomolecular pump to remove previously dissolved species. The gases were tested in the following order: H_2, He, N_2, O_2, CH_4, and CO_2, and a second test was performed on O_2 and N_2 to analyse the possible influence of the exposure to CO_2 on the transport properties.

The pressure in the fixed permeate volume was monitored using a pressure transducer, starting from the instant of exposure of the membrane to the feed gas. The permeability coefficient, P, was calculated from the slope of the time-pressure curve under steady-state conditions (eqn (1)) as follows:

$$p_t = p_0 + \left(d_p/d_t\right)_0 \cdot t + \frac{RT \cdot A}{V_p \cdot V_m} \cdot \frac{P_f \cdot P}{l}\left(t - \frac{l^2}{6D}\right) \quad (1)$$

where p_t is the permeate pressure at time t, p_0 the starting pressure, $(d_p/d_t)_0$ the baseline slope, P_f the feed pressure, R the universal gas constant, T the absolute temperature, A the exposed membrane area, V_p the permeate volume, and V_m the molar volume of the permeating gas at standard temperature and pressure (273 K and 1 atm). The term $p_0 + (d_p/d_t)_0$ accounts for the starting pressure and the baseline slope and is normally negligible in the case of well-evacuated defect-free samples. The time lag method was applied to determine the diffusion coefficient, D, of each gas through the membranes, according to (eqn (2)):

$$D = \frac{l^2}{6\theta} \quad (2)$$

where l is the membrane thickness and θ is the gas time lag. Assuming the validity of the solution-diffusion transport mechanism, the solubility coefficient, S, was obtained indirectly using (eqn (3)):

$$S = P/D \quad (3)$$

The detailed procedures are reported elsewhere.[28]

Results and discussion

Structural and textural characterisation of MOFs

MOF-801 and MIP-203 were synthesised following the procedures already reported in the literature and described in the experimental section.[18,29] The success of the syntheses was verified by acquiring the PXRD patterns of the MOF powders after the washing procedure (Fig. S1). As expected, the patterns are clearly distinct, reflecting the different topologies of the two MOFs. Specifically, MIP-203 exhibits a less densely connected structure, formed by 10-connected Zr_6 SBUs, compared to the 12-connected Zr_6 SBUs typical of MOF-801 (see crystal structures in Fig. S2). This reduced connectivity results in the more flexible framework of MIP-203.[18]

The structure of the two MOFs was also investigated at atomic level by ^{1}H and ^{13}C SSNMR spectroscopy. The ^{1}H DE MAS spectrum of activated MOF-801 shows a peak at 7.2 ppm assigned to the fumarate protons and peaks at 2.2 and 2.8 ppm assigned to the –OH groups (Fig. S3). In the ^{1}H–^{13}C CP MAS spectrum, vinyl carbons of fumarate resonate at 137.0 ppm, while the peak of the carboxylate carbons is observed at 171.0 ppm (Fig. 1). These findings agree with those reported by Zhang *et al.*[30]

The ^{1}H DE MAS NMR spectrum of activated MIP-203 shows signals at 7.3 and 9.0 ppm ascribed to the protons of fumarate and formate linkers, respectively, together with additional peaks at 2.4 and 3.2 ppm ascribed to the protons of the –OH groups (Fig. S3). The ^{1}H–^{13}C CP MAS spectrum displays a signal at 137.6 ppm ascribed to the vinyl carbons of fumarate and four distinct resonances in the carboxylate region at 167.7, 168.3, 169.7, and 170.4 ppm (Fig. 1), in general agreement with Wang *et al.*[18] The different carboxylate signals are better resolved with the aid of ^{1}H–^{13}C CP MAS spectra acquired at various contact times (from 0.1 ms to 4 ms; Fig. S4) and assigned through 2D ^{1}H–^{13}C HETCOR spectra that show cross-peaks between the signals of protons and nearby carbon atoms. In particular, in the spectrum acquired with a short contact time of 0.2 ms (Fig. S5a), cross-peaks are observed between carbons and bound or very close in space protons, while in the spectrum acquired with a contact time of 2 ms (Fig. S5b), cross-peaks are also observed between carbons and protons at longer distances. According to the ^{1}H–^{13}C HETCOR spectra, ^{13}C peaks at 167.7, 168.3, and 169.7 ppm are attributed to the carboxylate carbons of formate linkers, while the signal at 170.4 ppm is assigned to the carboxylate carbons of fumarate. The ^{1}H–^{13}C HETCOR spectra also reveal that the –OH protons resonating at 2.4 ppm are spatially close to the carboxylate groups of both formate and fumarate linkers, while those at 3.2 ppm are close to fumarate carboxylate groups.

To elucidate the impact of the different framework topologies on CO_2 adsorption performances, the textural properties of the two materials were investigated by measuring N_2 adsorption/desorption isotherms at 77 K (Fig. 2a).

As expected from the literature,[18,31] the two materials exhibit a markedly different N_2 uptake at saturation, indicative of the higher porosity and specific surface area of MOF-801 with respect to MIP-203. Specifically, the SSA_{BET} is 970 ± 3 $m^2\ g^{-1}$ for MOF-801 and 395.1 ± 4 $m^2\ g^{-1}$ for MIP-203. The goodness of the BET plots is reported in Fig. S6. The SSA_{BET} of MOF-801 is in good agreement with that reported in the literature for the MOF obtained *via* hydrothermal synthesis (1025 $m^2\ g^{-1}$),[31] which typically exhibits a higher surface area than its solvothermally prepared counterpart, using dimethylformamide as the solvent.[31] The larger SSA is commonly attributed to a higher degree of defectivity typical of materials synthesised in water, which implies the occurrence of missing clusters and, therefore, the formation of larger cavities.[32,33] In contrast, MIP-203 shows a slightly lower surface area than that reported in the literature.[18] This can be ascribed to the different particle morphology of MIP-203 presented in this work, characterised

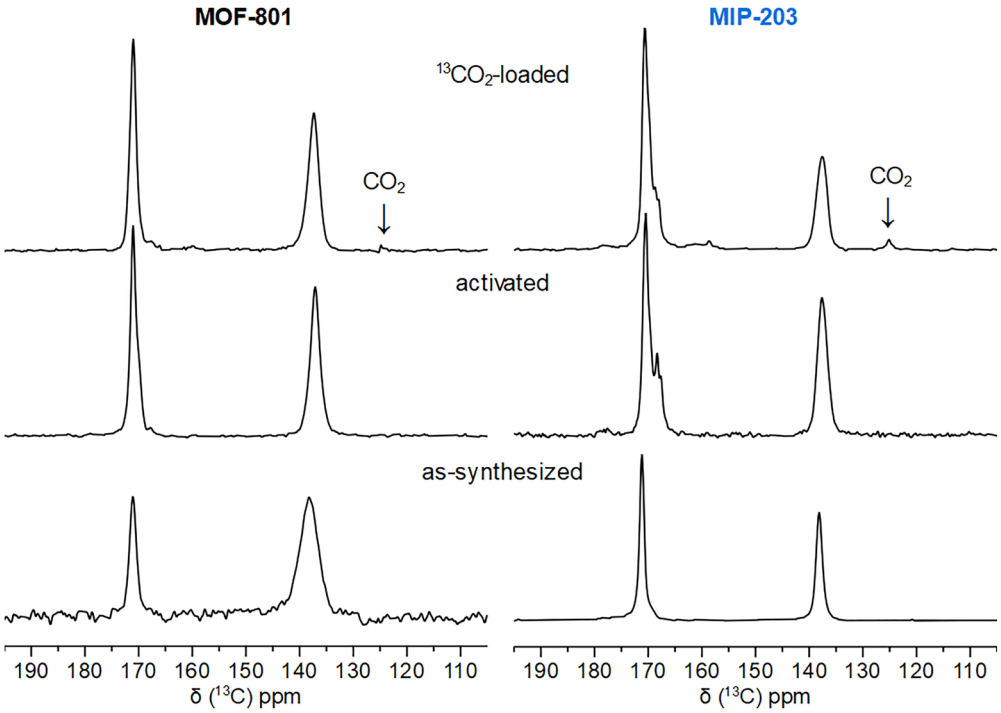

Fig. 1 $^{1}H-^{13}C$ CP MAS NMR spectra of as-synthesized, activated, and $^{13}CO_2$-loaded MOF-801 (left) and MIP-203 (right). All the spectra were recorded at 298 K using a spinning frequency of 15 kHz.

by smaller crystallites (see Fig. S7B) than the ones reported by Wang *et al.* (*ca.* 0.2 μm *vs.* 10–20 μm of length). This morphological variation likely arises from the use of sonication during synthesis, rather than conventional magnetic stirring. Despite the reduced crystallite size, MIP-203 remains morphologically different from MOF-801, which consists of nearly spherical nanoparticles (Fig. S7A).

The high degree of defectivity of MOF-801 synthesized in this work is further supported by pore analysis. From the crystallographic data, MOF-801 synthesised in dimethylformamide is characterized by two tetrahedral cavities (4.8 and 5.6 Å) and a larger octahedral cavity (7.4 Å).[34] This pore size is reproduced by the calculations performed with ZEO++[35] on the crystallographic structure reported in the literature (see Fig. S8A). The pore size distribution obtained by NL-DFT analysis identifies the two pore families, although with broader distributions (centred at 6 and 10 Å). The relationship between defectivity and textural properties in MOF-801 has been previously discussed by Cho *et al.*, who reported an increase in pore size, SSA_{BET}, and V_{TOT} for the material synthesized in H_2O (Zr-fum HT) compared to the reference sample prepared in dimethylformamide ($MOF\text{-}801_{ref}$).[31] All porosity-related parameters for MOF-801 materials reported in

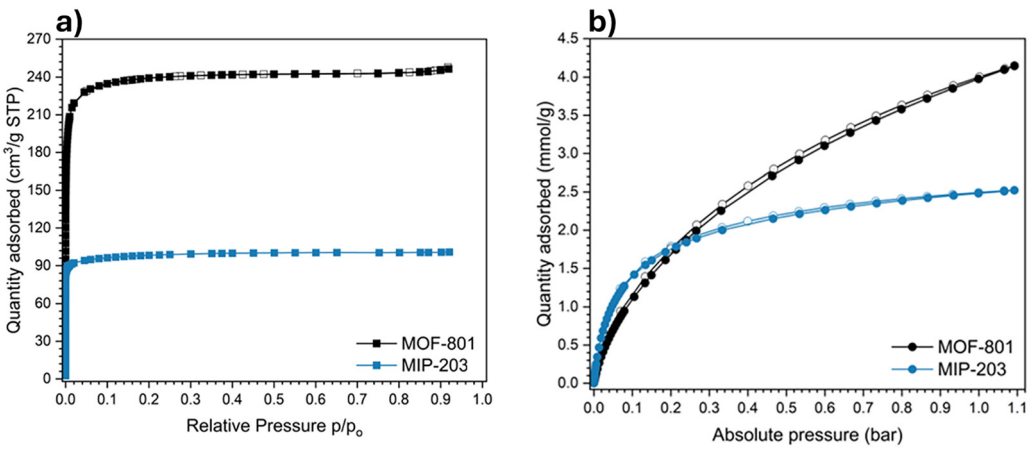

Fig. 2 (a) Adsorption (full symbols) and desorption (empty symbols) N_2 isotherms collected at 77 K on MOF-801 (black) and MIP-203 (blue). Desorption branch was not collected for MIP-203 due to the excessively long acquisition time. (b) CO_2 adsorption (full symbols) and desorption (empty symbols) isotherms collected at 273 K on MOF-801 (black) and MIP-203 (blue).

the literature and in this work are summarized in Table S1. The MOF-801 sample presented in this study exhibits intermediate properties between the two materials reported by Cho *et al.*[36] The higher defectivity observed in Zr-fum HT compared to the MOF-801 reported here may be attributed to the differences in the synthesis scale (milligrams in this work *versus* tens of grams in the reference study), which can influence the defectivity of the final product. A water-based synthetic approach was also reported by Jahan *et al.*[36] In that work, MOF-801 samples were synthesized using the sonication temperature as the variable parameter. Their pore analysis results (also summarized in Table S1) further support the use of textural property measurements as a tool to gain insights into the defectivity of the MOF-801 topology.

For MIP-203, crystallographic analysis indicates the presence of larger cavities of 5.2 Å connected by narrower apertures of 3.6 Å. This bimodal pore distribution is again confirmed by ZEO++ calculations (Fig. S8B).[19] In this case, NL-DFT pore analysis shows better agreement with the theoretical porosity, suggesting a lower degree of defect-induced porosity in this material. However, the pore sizes derived from NL-DFT calculations are systematically larger (about 1 Å) than those expected from theory. All the differences detected between the NL-DFT analysis and the crystallographic data can be due to the intrinsic limitations of the N_2 probe at 77 K, including restricted diffusion in ultramicropores and specific adsorbate-framework interactions.[37] Additional deviation may arise from the kernel choice for the NL-DFT analysis, despite the good agreement between the experimental and the theoretical isotherms (Fig. S9).

CO_2 adsorption mechanism in MOFs

Due to their distinct topology, arising from the different connectivity of the Zr-based SBUs, MOF-801 and MIP-203 are expected to display very different adsorption properties. In particular, MIP-203 exhibits a dynamic structural response to guest solvent removal (such as desorption of H_2O during activation), as previously documented by Wang *et al.*[18] Combined with its narrower pores not easily accessible to larger adsorbates, this behaviour could enhance its separation performance with respect to MOF-801 (and despite the higher accessible surface area of the latter MOF).

The CO_2 adsorption isotherm of MOF-801 at 273 K (black curve, Fig. 2b) is in line with literature reports for hydrothermally synthesised samples, with a CO_2 uptake at saturation of about 4 mmol g^{-1}.[38] Notably, the isotherm does not reach a plateau as the pressure approaches 1 bar, suggesting that only a fraction of the available pore volume is filled with CO_2 under these conditions, likely due to the relatively large cavities of the MOF. On the other hand, MIP-203 exhibits a different adsorption profile (blue curve, Fig. 2b). As expected, this MOF reaches a lower CO_2 uptake of $\sim$2.5 mmol g^{-1} at 1 bar, with the isotherm approaching the plateau at the upper bound of the pressure range, suggesting the complete filling of its smaller cavities.[18] Interestingly, at low CO_2 coverage, MIP-203 exhibits a steeper initial CO_2 uptake than MOF-801, reflecting stronger adsorbate-framework interactions and/or, equally, an enhanced confinement effect within the narrower pores of MIP-203. The second hypothesis is enforced by the early onset of saturation of this isotherm, indicating that adsorption predominantly occurs within a limited and energetically favourable pore network.

According to the previous work, MIP-203 displays a certain degree of flexibility when exposed to specific adsorbates.[18] To probe the structural dynamics of the MIP-203 framework during the adsorption/desorption of guest molecules (*i.e.* H_2O removal during activation and adsorption of CO_2), *ex situ* PXRD measurements were performed on as-synthesised, thermally activated, and CO_2-loaded (0.5 bar of CO_2 at room temperature) MIP-203 powder samples contained in three different capillary tubes. The diffraction patterns are shown in Fig. 3. Upon thermal activation (373 K overnight under dynamic vacuum), a small shift ($\sim$0.2°) of the main reflection towards higher angles is observed, indicating a slight contraction of the cell volume. This behaviour confirms, in agreement with previous reports,[18] that H_2O desorption can trigger a certain mobility of the framework. On the other hand, the pattern acquired under 0.5 bar of CO_2 closely resembles that of the activated sample, indicating that CO_2 adsorption does not induce significant reopening of the framework under these operating conditions. This suggests that, at variance with water, the interaction of CO_2 with the pore environment is not strong enough to trigger a cooperative structural response.

Interactions of the MOFs with water or CO_2 and adsorption-induced structural changes were also investigated at the atomic scale by ^1H and ^{13}C SSNMR measurements. The comparison of the ^1H DE MAS NMR spectra recorded for the as-synthesized and activated MIP-203 samples (Fig. S3) shows a shift of the signals of the fumarate and formate linkers at higher chemical shift values in the presence of physisorbed water, which exhibits a broad peak centred at 5.5 ppm. The adsorption of water

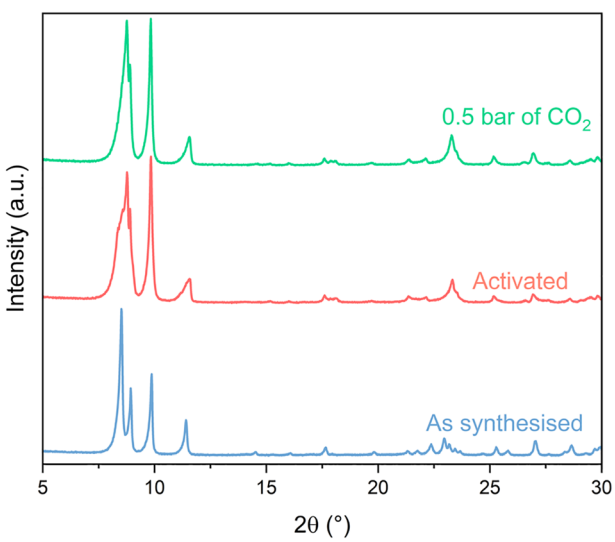

Fig. 3 PXRD patterns of the as-synthesised MIP-203 (blue curve), after thermal activation under vacuum (orange curve) and loaded with 0.5 bar of CO_2 (green curve).

also results in a shift of the signals of the vinyl carbons of fumarate (from 137.6 to 138.1 ppm) and of the carboxylate carbons of fumarate and formate linkers in the $^{1}H–^{13}C$ CP MAS spectra (Fig. 1). In particular, a single peak is observed for the carboxylate carbons of both linkers in the spectrum of as-synthesized MIP-203, at variance with the multiple signals observed for the activated sample. These findings are in agreement with the slight structural rearrangements involving the carboxylate groups and the alkenyl chain of fumarate observed by small shifts of the carboxylate stretching band and the –CH wagging band in C–C═C–C in the Raman spectra by Wang *et al.*[18]

The CO_2 loading results in broadening and chemical shift variations of the OH signals in the ^{1}H DE MAS spectrum of MIP-203 (Fig. S3), suggesting interactions between the hydroxyl groups and the CO_2 molecules, while only minor changes are observed for the signals of formate and fumarate. Accordingly, no significant shifts are observed for the carbon signals of the MIP-203 linkers (Fig. 1), supporting the absence of a structural response of the framework to CO_2 adsorption inferred by PXRD measurements. A weak resonance ascribed to the CO_2 carbon appears at 125.1 ppm in the $^{1}H–^{13}C$ CP MAS spectrum of the $^{13}CO_2$-loaded sample (1 bar at 298 K), indicating the presence of interactions of CO_2 with spatially close linker protons that allow magnetization transfer to CO_2 carbon. Further insights are provided by the $^{1}H–^{13}C$ HETCOR spectrum shown in Fig. S10, which reveals more intense cross-peaks between the CO_2 carbon and the formate proton with respect to those between the CO_2 carbon and fumarate protons. This proves that CO_2 mainly interacts with formate linkers and, to a lesser extent, with fumarate moieties, as observed for other gases.[19,39]

For MOF-801, the comparison between the ^{1}H DE MAS spectra of the as-synthesised and activated samples (Fig. S3) indicates the effective removal of adsorbed water and residual solvent upon activation, with only minor changes in the signal of fumarate protons at 7.2 ppm. The $^{1}H–^{13}C$ CP MAS NMR spectrum shows a slight shift of the carbons in the vinyl group of fumarate upon activation (from 137.9 to 137.0 ppm), while the peak of the carboxylate carbons remains at about 171 ppm (Fig. 1). Upon CO_2 loading, no significant changes are observed in the ^{1}H and ^{13}C signals of the fumarate linkers of MOF-801, whereas the proton signals of the OH groups slightly broaden and shift (Fig. S3), suggesting interactions of the gas with the OH groups, in agreement with *in situ* DRIFTS experiments reported by Li *et al.*,[9] showing an increase in the intensity of the $\nu_{as}(CO_2)$ vibration at 2342 cm^{-1} and the $\nu_{as+\nu s}$ vibration at 3699 cm^{-1} upon CO_2 adsorption ascribed to the binding effect between CO_2 and μ_3-OH groups. Moreover, in the $^{1}H–^{13}C$ CP MAS spectrum, a weak signal is detected at 124.9 ppm and assigned to the $^{13}CO_2$ carbon, indicating weak interactions of the gas with the framework.

The signal of $^{13}CO_2$ can be selectively observed by recording ^{13}C DE NMR spectra with a short recycle delay of 5 s (Fig. S11), in which the signals of the linker carbons are suppressed due to their long longitudinal relaxation times. A signal is observed in the spectrum of both CO_2-loaded MOF-801 and MIP-203 with an isotropic chemical shift, δ_{iso}, of 124.9 and 125.1 ppm, respectively, slightly broader for MIP-203.

To investigate how the MOF topology and framework–adsorbate interactions affect CO_2 dynamics, the ^{13}C DE spectra were also recorded under static conditions at variable temperatures for MOF-801 and MIP-203 loaded with $^{13}CO_2$. The line shape of the $^{13}CO_2$ signal arises from the average of the anisotropy of the chemical shift (CSA) interaction by the gas molecular motions in the framework.

For MOF-801, the spectra exhibit an isotropic, quite narrow signal centred at 124.9 ppm, the same δ_{iso} value observed in the ^{13}C DE MAS spectrum (Fig. S11), at all the investigated temperatures between 243 K and 298 K (Fig. 4), indicating that fast random motions of the gas molecules in the framework average out the CSA of the $^{13}CO_2$ carbon. This behaviour hints at weak interactions of CO_2 with the MOF-801 framework and is compatible with the high symmetry and large dimensions of the cavities, possibly increased by the presence of defects, in agreement with the shape of the adsorption isotherm.

On the other hand, for MIP-203, the ^{13}C static spectra in the 268–338 K range (Fig. 5) show a profile ascribed to CO_2 confined in the framework. An additional weak isotropic signal appears at 125.1 ppm above 278 K, showing a progressive increase in the intensity upon heating, most probably due to CO_2 outside the framework. The line shape of the main

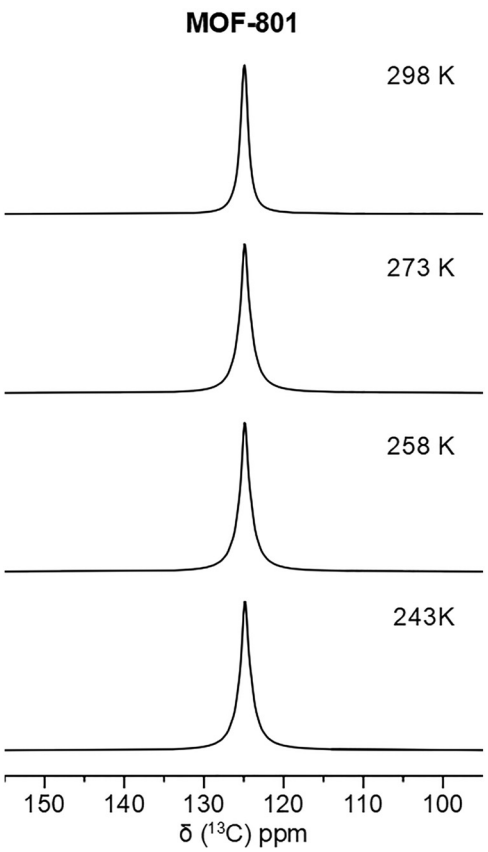

Fig. 4 ^{13}C DE static NMR spectra of $^{13}CO_2$ in MOF-801 at the indicated temperatures.

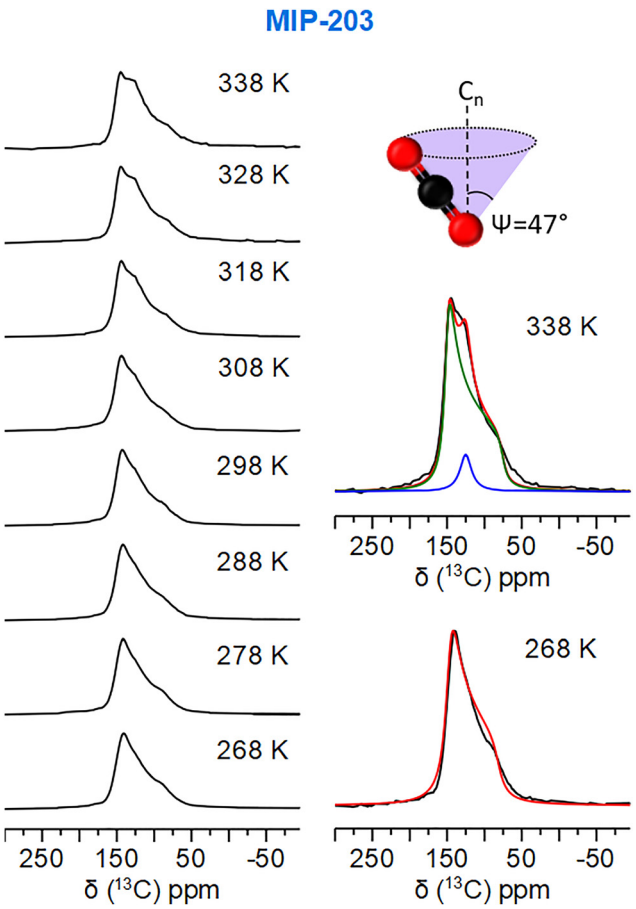

Fig. 5 ^{13}C DE static NMR spectra of $^{13}CO_2$ in MIP-203 at the indicated temperatures. Experimental spectra are shown in the left column. Simulated spectra at 268 and 338 K are shown on the right. The anisotropic line shapes were simulated considering a reorientational motion in a cone about a C_n axis ($n \geq 3$) in the fast regime, with the axis forming an angle of 47° with the CO_2 C_∞ axis, as sketched on the top.

anisotropic signal slightly changes with temperature and is characterized by an isotropic chemical shift, δ_{iso}, of 125.1 ppm, a span, Ω, of about 64 ppm, and a skew, κ, of 1 (Fig. 5), where $\delta_{iso} = (\delta_{11} + \delta_{22} + \delta_{33})/3$, $\Omega = \delta_{11} - \delta_{33}$, and $\kappa = 3(\delta_{22} - \delta_{iso})/\Omega$ according to the Maryland notation. δ_{11}, δ_{22}, and δ_{33} are the principal components of the chemical shift (CS) tensor, with $\delta_{11} \geq \delta_{22} \geq \delta_{33}$ (Mehring notation).[40] The same value of δ_{iso} is observed for CO_2 in the ^{13}C DE MAS spectrum of the same sample (Fig. S11). The span measures the breadth of the powder pattern and quantifies the extent of CSA, while the skew, ranging from −1 to 1, gives a measure of the symmetry of the CS tensor (with both ±1 values indicating axial symmetry). Therefore, the line shape of the main CO_2 signal indicates that the CSA is only partially averaged by the restricted motions of the gas molecules within the framework, arising from specific interactions and/or steric hindrance, as indeed suggested by the isotherm profile. The span reduction compared to fully immobilised CO_2, for which we considered Ω = 323 ppm and κ = 1,[24,25] indicates that a motion with a rate higher than the spectral broadness in frequency units occurs for CO_2 in the MOF at the investigated temperatures. Wobbling on an individual adsorption site and hopping between symmetry equivalent adsorption sites have been found for CO_2 in other MOFs by ^{13}C SSNMR spectroscopy.[41–46] The positive value of κ suggests that a wobbling or hopping motion occurs with an angle (ψ) between the C_∞ symmetry axis of CO_2 and the motion axis smaller than the magic angle (54.74°), while the axial line shape (κ = 1) indicates a 3-fold or higher symmetry for the motion, which should occur in the fast regime.[47,48] A satisfactory simulation of the spectral line shape (Fig. 5) can indeed be obtained at all the investigated temperatures with a reorientation in a cone motion among 3 equivalent sites in the fast regime with ψ = 47°. It is worth noting that this motion could be associated either with a reorientation of CO_2 about a local axis or with the hopping of CO_2 molecules among equivalent adsorption sites, also in combination with translation. The occurrence of both kinds of motions cannot be excluded. The substantial lack of changes in the anisotropic main signal on heating suggests that interactions of CO_2 with the MIP-203 framework are only slightly affected by temperature. This behaviour is consistent with the limited temperature dependence observed in the adsorption isotherms, as reported by Wang *et al.*[18] Spectral line shape simulations indicate that the relative amount of CO_2 inside the framework decreases from 100% at 268 K to 84% at 338 K.

The direct comparison between the ^{13}C static spectra of $^{13}CO_2$ in MIP-203 and MOF-801 (Fig. 4 and 5) suggests that, although interactions with the linkers are inferred from the observation of the $^{13}CO_2$ signal in the ^{13}C CP spectra for both MOFs, a preferential orientation and restricted motions of the gas molecules in the framework occur only in MIP-203. The different behaviour of CO_2 in the two MOFs can be rationalised by considering the different sizes and shapes of the pores, as well as the presence of different sites for interactions. MOF-801 has relatively large, highly symmetric cavities compared to the CO_2 kinetic diameter (3.3 Å), and interactions most probably occur only with the μ_3-OH groups. On the other hand, MIP-203 exhibits narrower, triangular channels where confinement effects are more pronounced and additional interactions with bridging formate linkers and, to a lesser extent, with fumarate linkers are possible, as inferred from the HETCOR experiment (Fig. S10).

Structural, morphological and gas transport properties of MMMs

To correlate the CO_2 adsorption and dynamic behaviour in MOF-801 and MIP-203 to their performance in MMMs, the two materials were incorporated into a PIM-1 matrix. The obtained MMMs, indicated as PIM-1/MOF-801 and PIM-1/MIP-203, were characterised by SEM combined with EDS to evaluate the dispersion and distribution of the two inorganic fillers within the polymeric matrix (Fig. S12). The SEM images on the surface of the PIM-1/MOF-801 show that the MOF is homogeneously dispersed in the membrane (Fig. S12A), as revealed by EDS analysis. On the other hand, the cross section of PIM-1/MIP-203 reveals a tendency to sediment, as shown by the EDS analysis

reported in Fig. S12C. Despite this sedimentation, the filler appears to remain uniformly distributed throughout the membrane bulk, as also confirmed by the SEM images of the membrane surfaces (Fig. S12A and B). Therefore, the transport properties are considered representative of the overall membrane and allow a meaningful comparison with the PIM-1/MOF-801 MMM.

^{1}H DE MAS (Fig. S13) and ^{1}H–^{13}CP MAS (Fig. S14) NMR spectra were recorded for the activated PIM-1/MOF-801 and PIM-1/MIP-203 MMMs to investigate their structural properties, also in comparison with the corresponding spectra recorded for activated PIM-1. The ^{1}H DE MAS spectra are dominated by signals arising from the aliphatic (1.6 ppm) and aromatic (7.1 ppm) protons of the PIM-1 matrix, and show very weak signals from the MOF linker protons (Fig. S13). Correspondingly, the ^{1}H–^{13}C CP MAS spectra show intense signals ascribed to the PIM-1 carbons and weak resonances from carbons of linkers (Fig. S14).

Gas transport properties of the MMMs after methanol treatment and subsequent aging are reported in Table 1 and Table S2. The methanol-treated PIM-1/MOF-801 membrane does not exhibit any enhancement in permeability for either CO_2 or light gases compared to neat PIM-1 (Table 1). In fact, the CO_2 permeability is approximately 10 500 Barrer for both samples, and also the permeabilities of light gases remain comparable to those of neat PIM-1 (H_2: approx. 4500 Barrer; He: approx. 1900 Barrer), which are typical values for freshly treated PIM-1 with low chain branching. Similarly, the selectivity values for the investigated gas pairs are virtually the same of the neat polymer (Fig. 6), indicating a limited impact of MOF-801 incorporation on the transport properties of the resulting MMM. In contrast, the MMM containing MIP-203 shows a modest increase in CO_2 permeability after methanol treatment, up to about 11 500 Barrer, together with a stronger enhancement in H_2 and He permeabilities, which increase to approximately 5500 Barrer and 2250 Barrer, respectively. The effect of MIP-203 is better analysed by decoupling the permeability in the diffusivity and solubility terms. Fig. S15A reports the gas diffusion coefficient (D) as a function of the squared effective diameter (d_{eff}^2) for O_2, CO_2, N_2 and CH_4 in PIM-1/MOF-801 and PIM-1/MIP-203 MMMs and in a neat PIM-1 membrane. For all membranes, a linear trend in semi-logarithmic coordinates is observed, similarly to what is expected for polymers. The inclusion of MOF-801 does not significantly alter the transport properties of the PIM-1 matrix. Instead, PIM-1/MIP-203 exhibits higher gas diffusion coefficients than those of neat PIM-1 and PIM-1/MOF-801. This is further supported by the trends of solubility as a function of the square of the critical temperature (T_c^2) shown in Fig. S15B, where a clear overlap of the curves related to neat PIM-1 and PIM-1/MOF-801 is observed. Gas sorption in the PIM-1/MIP-203 membrane is slightly lower than that of the other two membranes, confirming that the increase in permeability is primarily driven by enhanced diffusion.

Table 1 Permeability (P) of the neat PIM-1, PIM-1/MOF-801 and PIM-1/MIP-203 membranes evaluated at 308 K. Numbers in brackets refer to the aging time (in days) of the membranes after methanol treatment

	P [Barrer]					
Membrane	N_2	O_2	CO_2	CH_4	H_2	He
PIM-1	673	1983	10 761	1125	4563	1838
PIM-1/MOF-801	632	1859	10 421	1070	4696	1940
(27 days)	520	1609	8564	795	4231	1729
(92 days)	408	1357	6991	602	3836	1640
PIM-1/MIP-203	767	2221	11 676	1130	5495	2261
(27 days)	685	2074	9605	1045	5513	2388
(95 days)	348	1107	5455	426	3317	1520

As typically observed for PIM-based membranes, ageing of MMMS leads to a reduction in permeability accompanied by an increase in selectivity with respect to the freshly treated membranes. This follows the permeability–selectivity trade-off typically observed in Robeson plots (Fig. 6). The CO_2 permeability in PIM-1/MOF-801 is reduced to about 35% after long ageing, in agreement with the literature data, where a reduction of 30% was measured after 100 days of ageing.[15] Small differences between data herein reported and literature results can be ascribed to the differences in the synthesis of the PIM-1 matrix, as well as to sample history. In contrast, in the early stage of physical ageing, PIM-1/MIP-203 undergoes a rearrangement of the polymer chains that, apparently, leads to a temporary enlargement of the smaller bottlenecks between the free-volume elements. This effect produces a significant increase in permeability only for very light gases (*i.e.*, H_2 and He),[49] whereas it decreases for other gases. A similar behaviour was previously observed for the neat PIM-1 membranes.[50,51]

Dynamics of CO_2 in MMMs

^{13}C SSNMR spectroscopy was employed to investigate the interactions and dynamics of CO_2 in the PIM-1/MOF-801 and PIM-1/MIP-203 MMMs, exploiting $^{13}CO_2$ loaded on the membranes at 1 bar pressure (298 K). A very weak signal is observed at 124.9 ppm for the CO_2 carbon in the ^{1}H–^{13}C CP MAS spectra of both membranes (Fig. S14), while no changes are observed for the carbon signals of PIM-1 and MOFs upon CO_2 loading, indicating that weak interactions occur between the MMM matrices and the gas. To study CO_2 dynamics in the two MMMs, ^{13}C DE spectra were acquired at 298 K under static conditions. In both cases, the spectra are dominated by an isotropic signal at 124.9 ppm arising from CO_2 undergoing fast random motions within the polymeric matrix of the MMM, as in PIM-1 (Fig. S16). However, a closer inspection of the base of this signal (Fig. 7) reveals distinct features for the two MMMs. For PIM-1/MIP-203, a broad peak with an anisotropic shape similar to that observed for pristine MIP-203 is detected, whereas the spectrum of PIM-1/MOF-801-F exhibits the sole isotropic CO_2 signal and the same signals observed for the PIM-1 membrane. This is consistent with the behaviour of CO_2 in pristine MOF-801. These results suggest that the dynamics of CO_2 is similar in the MOFs alone and embedded in the PIM-1 polymeric matrix.

For MIP-203/PIM-1, the relative CO_2 content in the MOF and polymer was estimated by deconvolution of the static ^{13}C spectrum (Fig. 7 and Fig. S16). Although the deconvolution

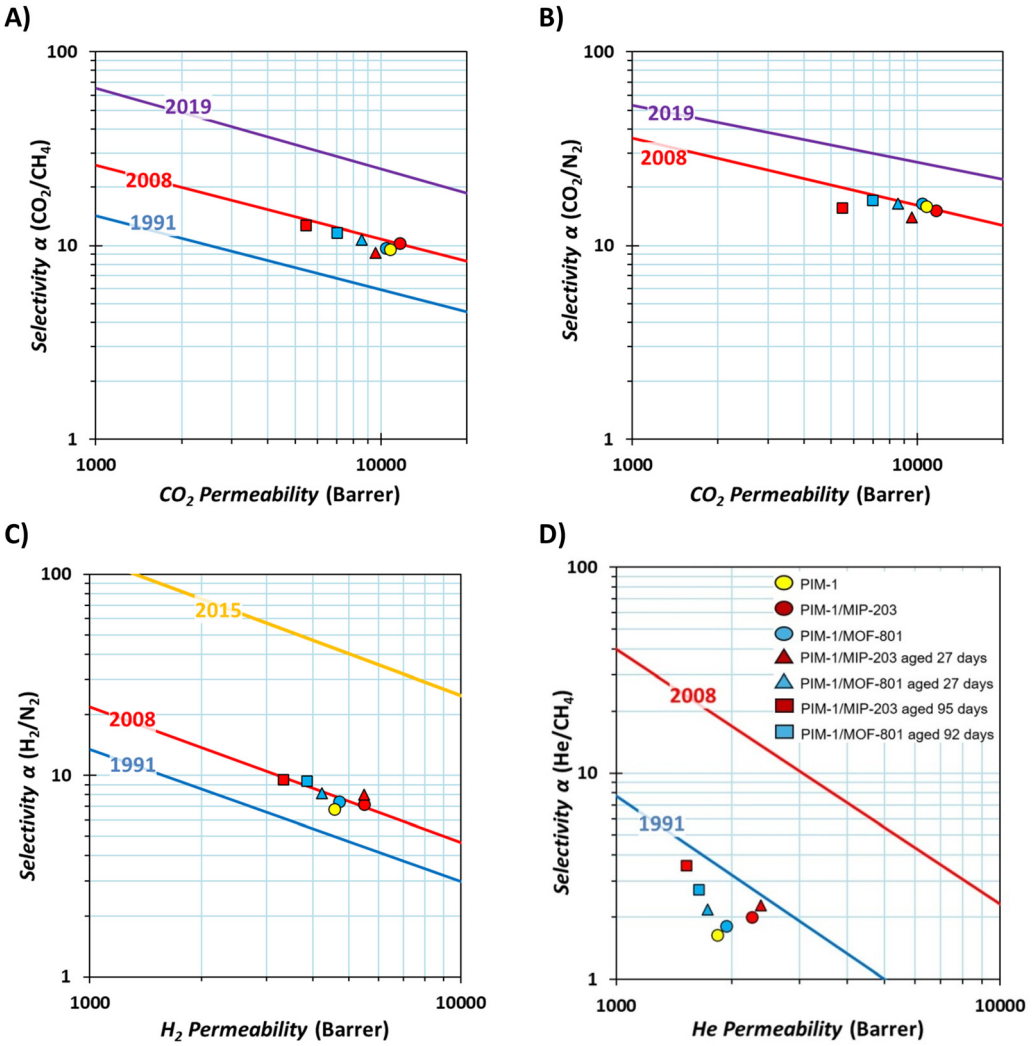

Fig. 6 Robeson diagrams for the gas pairs (A) CO_2/CH_4, (B) CO_2/N_2, (C) H_2/N_2, and (D) He/CH_4. The upper bounds are shown in blue (1991),[52] red (2008), yellow (2015),[53] and purple (2019).[54] Gas permeabilities at 308 K are reported for PIM-1/MIP-203 (red) and PIM-1/MOF-801 (blue). Circles denote fresh samples treated with methanol, triangles represent samples aged for ~30 days, and squares represent samples aged for ~90 days. The neat PIM-1 polymer is included as a reference (yellow circle).

was not straightforward due to the presence of residual broad signals of the membrane carbons, we estimated that 8% ± 1% of the adsorbed CO_2 exhibits the characteristic anisotropic dynamics of MIP-203. By considering that a comparable amount of CO_2 per gram is adsorbed by MIP-203 (2.5 mmol g^{-1}) and PIM-1 (2.43 mmol g^{-1}) at 1 bar and that MIP-203 constitutes 10 wt% of the MMM, this result indicates a non-selective distribution of CO_2 between the MMM components (CO_2 isotherms collected at 273 K are reported in Fig. S17).

The relationship between the retained anisotropic CO_2 dynamics in MIP-203 and the enhanced diffusion coefficients measured for the corresponding MMM is not straightforward, since it also implies a consideration of MOF particle morphology and distribution/orientation in the polymer matrix and MOF/polymer interfacial behaviour. However, our results suggest that MIP-203 may provide preferential transport domains within the polymer matrix, leading to more efficient diffusive pathways and contributing to the enhanced gas diffusion observed experimentally for the MMM.

Conclusions

With the aim of unravelling how the topology of Zr-fumarate MOFs governs CO_2 adsorption properties and gas transport in MMMs, a comprehensive multi-technique investigation was carried out on MOF-801 and MIP-203 and the corresponding PIM-1-based MMMs. The combination of pore analysis, adsorption measurements, SSNMR spectroscopy, and membrane permeation experiments enabled direct correlation of local host–guest interactions and CO_2 dynamics with macroscopic transport behavior.

The different pore architecture of the two MOFs, consisting of quite large tetrahedral and octahedral cavities in MOF-801 and narrow one-dimensional channels in MIP-203, as confirmed

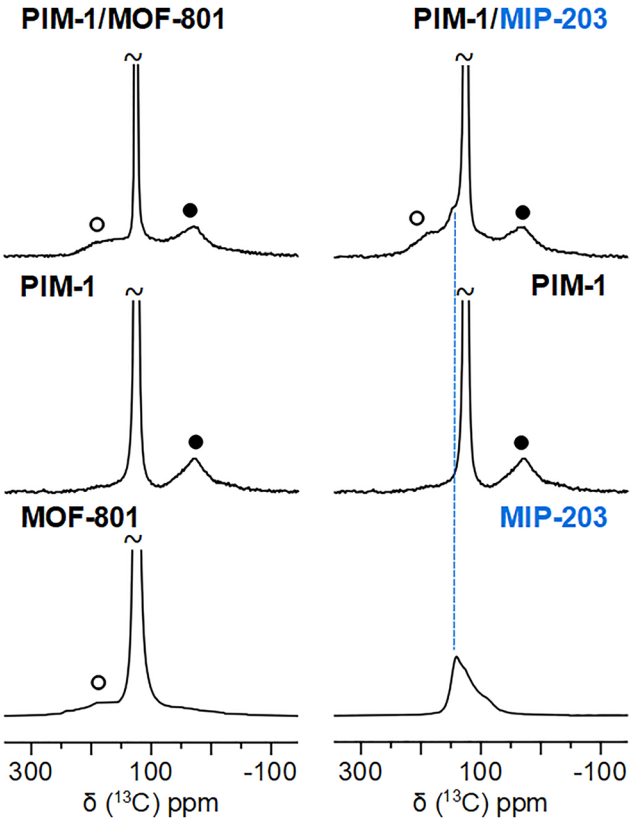

Fig. 7 Expansions of the ^{13}C DE static NMR spectra of $^{13}CO_2$ in (left) MOF-801, PIM-1, and PIM-1/MOF-801 and (right) MIP-203, PIM-1, and PIM-1/MIP-203, recorded at 298 K. Out-of-scale signals arise from CO_2 undergoing fast isotropic motions (see Fig. S16). Full and empty circles indicate broad signals from PIM-1 and MOFs, respectively.

by pore analysis, together with the different chemical environments generated by the linkers, resulted in differences in the CO_2 uptake and dynamics. In particular, SSNMR measurements highlighted preferential interactions of CO_2 with formate in MIP-203 and, to a lesser extent, with fumarate linkers, in addition to interactions with OH groups that were observed in both MOFs. The stronger confinement of CO_2 in MIP-203 channels led to anisotropic dynamics, most probably associated with localized motions of the gas molecules in the interaction sites, only slightly affected by temperature. On the other hand, the large and highly symmetric cavities of MOF-801 promoted fast isotropic motions of CO_2 molecules. At the macroscopic level, these differences translated into a much steeper low-pressure CO_2 adsorption isotherm for MIP-203 than that for MOF-801. The SSNMR results demonstrated that the CO_2 dynamics in the two MOFs is preserved after their incorporation into the polymeric PIM-1 matrix. Gas permeation measurements further highlighted a clear distinction of the diffusion and solubility coefficients between the two MMMs, arising from the combined effects of the MOF topology and different MOF/polymer interfacial interactions. In particular, although the inclusion of MOF-801 does not significantly affect the intrinsic transport properties of PIM-1, the incorporation of MIP-203 enhances gas permeability, particularly for smaller molecules. Upon ageing, all membranes exhibit the typical permeability selectivity trade-off, although PIM-1/MIP-203 shows a distinct behavior in the early stage, with a temporary stabilization or increase in permeability for the lightest gases.

Overall, this study demonstrates that subtle variations in the MOF topology and chemistry have a significant impact on CO_2 confinement, molecular dynamics and, ultimately, membrane transport properties. More broadly, the study highlights how the integration of advanced SSNMR characterization with adsorption and permeation analyses can provide useful guidelines for the rational design of novel MOF-based MMMs for gas separation applications.

Author contributions

V. G.: investigation, formal analysis, validation, writing – original draft, writing – review & editing, visualization; E. C.: investigation, formal analysis, validation, writing – original draft, writing – review & editing, visualization; L. T.: formal analysis, validation, writing – original draft, writing – review & editing; M. V.: formal analysis, validation, writing – original draft, writing – review & editing; F. D. C.: formal analysis, validation, writing – original draft; S. B.: formal analysis, validation, writing – original draft; M. C.: formal analysis, validation, writing – original draft, writing – review & editing; G. B.: formal analysis, validation, writing – original draft, writing – review & editing; A. F.: upervision, formal analysis, validation, writing – original draft, writing – review & editing, resources, funding acquisition; F. C.: conceptualization, supervision, formal analysis, validation, writing – original draft, writing – review & editing, resources, funding acquisition; L. C.: conceptualization, supervision, formal analysis, validation, writing – original draft, writing – review & editing, resources, funding acquisition; and V. C.: conceptualization, supervision, formal analysis, validation, writing – original draft, writing – review & editing, resources, funding acquisition.

Conflicts of interest

There are no conflicts to declare.

Data availability

Herein we declare that all the data reported in the manuscript "Impact of Framework Topologies on CO_2 Adsorption and Transport Properties in Zr-Fumarate Metal–Organic Frameworks and Their Mixed-Matrix Membranes" submitted to Materials Advances are original, and the datasets generated during this study are publicly available at Zenodo at the link https://doi.org/10.5281/zenodo.20393590.

Supplementary information (SI): additional PXRD patterns. Additional ^{1}H and ^{13}C MAS NMR spectra. SEM images and EDS analysis of MOF and membranes. Gas sorption and BET data treatment. Tables with gas diffusion coefficients as function of aging for MMM. See DOI: https://doi.org/10.1039/d6ma00781c.

Acknowledgements

All the authors have received funding from the European Union's Horizon Europe research and innovation program under grant agreement no. 101115488, within the EIC pathfinder project "DAM4CO$_2$", and from UK Research and Innovation (UKRI) under the UK government's Horizon Europe funding guarantee, grant number 10083164. V. C. has received funding from the Project CH4.0 under the MUR program "Dipartimenti di Eccellenza 2023–2027" (CUP: D13C22003520001).

References

1 K. Sumida, D. L. Rogow, J. A. Mason, T. M. McDonald, E. D. Bloch, Z. R. Herm, T.-H. Bae and J. R. Long, *Chem. Rev.*, 2012, **112**, 724–781.
2 H. Jasuja, J. Zang, D. S. Sholl and K. S. Walton, *J. Phys. Chem. C*, 2012, **116**, 23526–23532.
3 J. Fu and Y. Wu, *Chem. – Eur. J.*, 2021, **27**, 9967–9987.
4 T. O. Abodunrin, M. Kloda, J. Demel and M. Taddei, *Dalton Trans.*, 2023, **52**, 5865–5869.
5 S. Daliran, A. R. Oveisi, C.-W. Kung, U. Sen, A. Dhakshinamoorthy, C.-H. Chuang, M. Khajeh, M. Erkartal and J. T. Hupp, *Chem. Soc. Rev.*, 2024, **53**, 6244–6294.
6 P. G. M. Mileo, K. H. Cho, J.-S. Chang and G. Maurin, *Dalton Trans.*, 2021, **50**, 1324–1333.
7 P. Iacomi, F. Formalik, J. Marreiros, J. Shang, J. Rogacka, A. Mohmeyer, P. Behrens, R. Ameloot, B. Kuchta and P. L. Llewellyn, *Chem. Mater.*, 2019, **31**, 8413–8423.
8 H. Furukawa, F. Gándara, Y.-B. Zhang, J. Jiang, W. L. Queen, M. R. Hudson and O. M. Yaghi, *J. Am. Chem. Soc.*, 2014, **136**, 4369–4381.
9 C.-N. Li, S.-M. Wang, Z.-P. Tao, L. Liu, W.-G. Xu, X.-J. Gu and Z.-B. Han, *Inorg. Chem.*, 2023, **62**, 7853–7860.
10 N. Prasetya and K. Li, *Sep. Purif. Technol.*, 2022, **301**, 122024.
11 Y. Gu, B. A. Anjali, S. Yoon, Y. Choe, Y. G. Chung and D.-W. Park, *J. Mater. Chem. A*, 2022, **10**, 10051–10061.
12 M. Parsaei and K. Akhbari, *Inorg. Chem.*, 2022, **61**, 5912–5925.
13 V. V. Butova, I. A. Pankin, O. A. Burachevskaya, K. S. Vetlitsyna-Novikova and A. V. Soldatov, *Inorg. Chim. Acta*, 2021, **514**, 120025.
14 W. Chen, Z. Zhang, C. Yang, J. Liu, H. Shen, K. Yang and Z. Wang, *J. Membr. Sci.*, 2021, **636**, 119581.
15 W. Chen, Z. Zhang, L. Hou, C. Yang, H. Shen, K. Yang and Z. Wang, *Sep. Purif. Technol.*, 2020, **250**, 117198.
16 M. Ahmadi, S. Janakiram, S. Velioğlu, A. Lindbråthen, B. A. Grimes, M. Hillestad and L. Deng, *Carbon Capture Sci. Technol.*, 2024, **13**, 100307.
17 W. Dong, J. Yan, T. Ji, M. Wu, Y. Sun, Y. He, X. Li, K. Yu, B. Sun and Y. Liu, *J. Membr. Sci.*, 2024, **705**, 122946.
18 S. Wang, N. Xhaferaj, M. Wahiduzzaman, K. Oyekan, X. Li, K. Wei, B. Zheng, A. Tissot, J. Marrot, W. Shepard, C. Martineau-Corcos, Y. Filinchuk, K. Tan, G. Maurin and C. Serre, *J. Am. Chem. Soc.*, 2019, **141**, 17207–17216.
19 R. Chen, B. Sheng, F. Zheng, J. Li, H. Sun, F. Zhou, L. Chen, Z. Zhang, Q. Yang, Q. Ren and Z. Bao, *AIChE J.*, 2023, **69**, e18169.
20 P. M. Budd, E. S. Elabas, B. S. Ghanem, S. Makhseed, N. B. McKeown, K. J. Msayib, C. E. Tattershall and D. Wang, *Adv. Mater.*, 2004, **16**, 456–459.
21 J. Rouquerol, P. Llewellyn and F. Rouquerol, *Stud. Surf. Sci. Catal.*, 2007, **160**, 49–56.
22 R. K. Harris, E. D. Becker, S. M. Cabral de Menezes, R. Goodfellow and P. Granger, *Solid State Nucl. Magn. Reson.*, 2002, **22**, 458–483.
23 V. Macho, L. Brombacher and H. W. Spiess, *Appl. Magn. Reson.*, 2001, **20**, 405–432.
24 A. J. Beeler, A. M. Orendt, D. M. Grant, P. W. Cutts, J. Michl, K. W. Zilm, J. W. Downing, J. C. Facelli, M. S. Schindler and W. Kutzelnigg, *J. Am. Chem. Soc.*, 1984, **106**, 7672–7676.
25 C. R. Bowers, H. W. Long, T. Pietrass, H. C. Gaede and A. Pines, *Chem. Phys. Lett.*, 1993, **205**, 168–170.
26 M. R. Khdhayyer, E. Esposito, A. Fuoco, M. Monteleone, L. Giorno, J. C. Jansen, M. P. Attfield and P. M. Budd, *Sep. Purif. Technol.*, 2017, **173**, 304–313.
27 S. C. Fraga, M. Monteleone, M. Lanč, E. Esposito, A. Fuoco, L. Giorno, K. Pilnáček, K. Friess, M. Carta, N. B. McKeown, P. Izák, Z. Petrusová, J. G. Crespo, C. Brazinha and J. C. Jansen, *J. Membr. Sci.*, 2018, **561**, 39–58.
28 A. Fuoco, M. Monteleone, E. Esposito, R. Bruno, J. Ferrando-Soria, E. Pardo, D. Armentano and J. C. Jansen, *Computation*, 2020, **8**, 28.
29 M. Ganesh, P. Hemalatha, M. M. Peng, W. S. Cha and H. T. Jang, *Aerosol Air Qual. Res.*, 2014, **14**, 1605–1612.
30 W. Zhang, B. E. G. Lucier, V. Martins, T. Azizivahed, I. Hung, Y. Xu, Z. Gan, A. Venkatesh, T. W. Goh, W. Huang, A. J. Rossini and Y. Huang, *Phys. Chem. Chem. Phys.*, 2025, **27**, 4704–4716.
31 K. H. Cho, P. G. M. Mileo, J. S. Lee, U.-H. Lee, J. Park, S. J. Cho, S. K. Chitale, G. Maurin and J.-S. Chang, *ACS Appl. Mater. Interfaces*, 2021, **13**, 1723–1734.
32 M. V. Solovyeva, L. G. Gordeeva, T. A. Krieger and Yu. I. Aristov, *Energy Convers. Manage.*, 2018, **174**, 356–363.
33 M. Aghajani Hashjin, S. Zarshad, H. B. Motejadded Emrooz and S. Sadeghzadeh, *Sci. Rep.*, 2023, **13**, 16983.
34 F. Rouhani and M. Ghiasvand, *Microporous Mesoporous Mater.*, 2024, **366**, 112941.
35 T. F. Willems, C. H. Rycroft, M. Kazi, J. C. Meza and M. Haranczyk, *Microporous Mesoporous Mater.*, 2012, **149**, 134–141.
36 I. Jahan, T. H. Rupam, M. L. Palash, K. A. Rocky and B. B. Saha, *J. Mol. Liq.*, 2022, **345**, 117760.
37 T. Islamoglu, K. B. Idrees, F. A. Son, Z. Chen, S. J. Lee, P. Li and O. K. Farha, *J. Mater. Chem. A*, 2022, **10**, 157–173.
38 D. Morelli Venturi, M. S. Notari, R. Bondi, E. Mosconi, W. Kaiser, G. Mercuri, G. Giambastiani, A. Rossin, M. Taddei and F. Costantino, *ACS Appl. Mater. Interfaces*, 2022, **14**, 40801–40811.
39 R. Chen, J. Li, F. Zhou, B. Sheng, H. Sun, F. Zheng, Q. Yang, Z. Zhang, Q. Ren and Z. Bao, *Ind. Eng. Chem. Res.*, 2023, **62**, 13144–13152.

40 R. K. Harris, E. D. Becker, S. M. C. De Menezes, P. Granger, R. E. Hoffman and K. W. Zilm, *Magn. Reson. Chem.*, 2008, **46**, 582–598.
41 V. J. Witherspoon, J. Xu and J. A. Reimer, *Chem. Rev.*, 2018, **118**, 10033–10048.
42 Y. Fu, H. Guan, J. Yin and X. Kong, *Coord. Chem. Rev.*, 2021, **427**, 213563.
43 B. E. G. Lucier, S. Chen and Y. Huang, *Acc. Chem. Res.*, 2018, **51**, 319–330.
44 X. Kong, E. Scott, W. Ding, J. A. Mason, J. R. Long and J. A. Reimer, *J. Am. Chem. Soc.*, 2012, **134**, 14341–14344.
45 L.-C. Lin, J. Kim, X. Kong, E. Scott, T. M. McDonald, J. R. Long, J. A. Reimer and B. Smit, *Angew. Chem., Int. Ed.*, 2013, **52**, 4410–4413.
46 F. Nardelli, F. Nerli, E. Della Latta, F. Martini, M. Geppi, M. Taddei and L. Calucci, *J. Phys. Chem. C*, 2024, **128**, 6887–6896.
47 M. Inukai, T. Kurihara, Y. Noda, W. Jiang, K. Takegoshi, N. Ogiwara, H. Kitagawa and K. Nakamura, *Phys. Chem. Chem. Phys.*, 2020, **22**, 14465–14470.
48 R. M. Marti, J. D. Howe, C. R. Morelock, M. S. Conradi, K. S. Walton, D. S. Sholl and S. E. Hayes, *J. Phys. Chem. C*, 2017, **121**, 25778–25787.
49 A. Fuoco, C. Rizzuto, E. Tocci, M. Monteleone, E. Esposito, P. M. Budd, M. Carta, B. Comesaña-Gándara, N. B. McKeown and J. C. Jansen, *J. Mater. Chem. A*, 2019, **7**, 20121–20126.
50 P. Bernardo, F. Bazzarelli, F. Tasselli, G. Clarizia, C. R. Mason, L. Maynard-Atem, P. M. Budd, M. Lanč, K. Pilnáček, O. Vopička, K. Friess, D. Fritsch, Yu. P. Yampolskii, V. Shantarovich and J. C. Jansen, *Polymer*, 2017, **113**, 283–294.
51 M. Longo, M. K. Amin, M. Monteleone, P. Hajivand, A. Fuoco, C. Ye, J. C. Jansen and N. B. McKeown, *J. Membr. Sci.*, 2026, **749**, 125466.
52 L. M. Robeson, *J. Membr. Sci.*, 1991, **62**, 165–185.
53 R. Swaidan, B. Ghanem and I. Pinnau, *ACS Macro Lett.*, 2015, **4**, 947–951.
54 B. Comesaña-Gándara, J. Chen, C. G. Bezzu, M. Carta, I. Rose, M.-C. Ferrari, E. Esposito, A. Fuoco, J. C. Jansen and N. B. McKeown, *Energy Environ. Sci.*, 2019, **12**, 2733–2740.

